



Original Research

3D printing of an integrated triphasic MBG-alginate scaffold with enhanced interface bonding for hard tissue applications

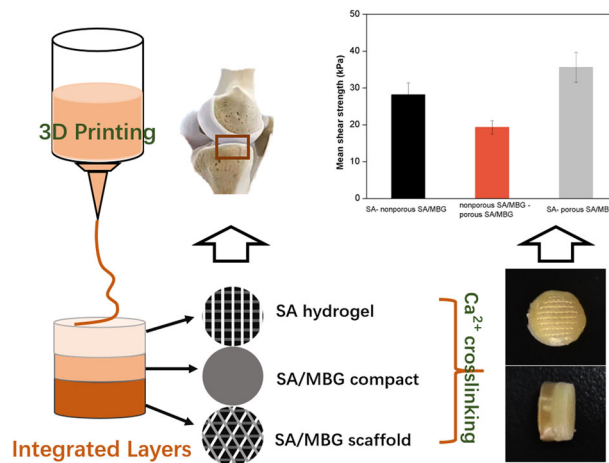
Min Zhu¹ · Xin He¹ · Chen Xin¹ · Yufang Zhu¹ · Zhongtang Liu²

Received: 5 December 2019 / Accepted: 27 October 2020 / Published online: 28 November 2020
© Springer Science+Business Media, LLC, part of Springer Nature 2020

Abstract

Osteochondral defects affect both of cartilage and subchondral areas, thus it poses a significant challenge to simultaneously regenerate two parts in orthopedics. Tissue engineering strategy is currently regarded as the most promising way to repair osteochondral defects. This study focuses on developing a multilayered scaffold with enhanced interface bonding through 3D printing. One-shot printing process enables control over material composition, pore structure, and size in each region of the scaffold, while realizes seamlessly integrated construct as well. The scaffold was designed to be triphasic: a porous bone layer composed of alginate sodium (SA) and mesoporous bioactive glasses (MBG), an intermediate dense layer also composed of SA and MBG and a cartilaginous layer composed of SA. The mechanical strength including the interface adhesion strength between layers were characterized. The results indicated that SA crosslinking after 3D printing anchored different materials together and integrated all regions. Additional scaffold soaking in simulated body fluid (SBF) and cell culture medium induced apatite deposition and had weakened the compressive and tensile strengths, while no layer dislocation or delamination occurred.

Graphical Abstract



1 Introduction

Osteochondral defects occur frequently from traumatic injuries to joint. Prolonged damages without healing result in osteoarthritis and decreased quality of life [1]. Generally, osteochondral tissues include an articular cartilage region and a subchondral bone region linking by a densified interface. Both of two regions are affected when osteochondral defects or disease arise [2]. Therefore, the cartilage zone, the interface layer, and sub-bone parts should be taken

✉ Min Zhu
mzhu@usst.edu.cn
✉ Zhongtang Liu
surgeon_liu@163.com

¹ School of Materials Science and Engineering, University of Shanghai for Science and Technology, Shanghai, PR China
² Department of Orthopedics, Changhai Hospital, Second Military Medical University, Shanghai, PR China

into considerations into therapies, which is seldomly satisfied via surgical treatments in clinic nowadays [3, 4].

A strategy of tissue engineering based on elaborately designed scaffolds emerged as an alternative recently [5]. Due to the lineage specific differences between cartilage and bone tissues, the TE scaffolds must provide distinct segregated support for two cell populations with proper biochemical and biomechanical microenvironments [6]. To mimic the complex and hierarchical structure of osteochondral tissues, layered multiphasic scaffolds are probably workable for synchronizing chondrogenesis and osteogenesis [7]. Thus, plenty of studies regarding to bilayer or multilayer scaffolds have been carried out. Pore structures, composition gradients, or biophysical cues of every scaffold layer were tailored according to natural osteochondral properties [8–10]. For example, the subchondral bone region needs interpenetrated pore channel and sufficient mechanical strength to bear high loading of joints, however, the cartilage region is always of much lower stiffness [11].

Although promising, the layered scaffolds are still far more optimal and quite a few limitations exist, such as time-consuming fabrication, lacking of individuality unstable interface joining and so on [7, 12]. Conventional fabrication techniques including freeze-drying [13], thermal-induced phase separation [14], or solvent leaching [15] hardly improve present scaffold functions. Furthermore, it is inevitable to utilize adhesives or wrapper integrating single layers [16, 17], which cause additional operative difficulties and biocompatibility issues. Challenges of sufficient interfacial strength also still remain among the first generation of multiphasic scaffolds. The high incidence of dislocation or delamination suggests that the joining strength is not enough when separate monophasic scaffolds were fused together by sutures or biological glues [18]. 3D printing recently has gained intensive interests in producing customized implants as well as TE scaffolds for patients [19, 20]. One of the most compelling utilization of 3D printing is embodied in multi-nozzle printing, which means a series of different materials or structures can be printed within one implant [21]. To date, a variety of bioceramics, polymers, and their composite materials were designed to serve as 3D printing inks to fabricate bone or cartilage generation scaffolds [22]. The selection of materials and structure design by 3D printing tailors the biological and mechanical response of a scaffold [23]. Hard bone tissue engineering scaffolds demand relatively high mechanical strength that can bear loads, hence, bioceramics, including calcium phosphate, calcium silicate and glass-ceramics, and their composites are usually applied [22, 24]. Thereinto, mesoporous bioactive glass (MBG) attract intensive interests due to excellent apatite formation ability and drug delivery function [25]. MBG are

degradable over time, and capable of promoting bone formation, releasing soluble silica and calcium ions for osteoconduction. As for cartilage scaffolds, polymers including both natural (collagen, hyaluronic acid, alginate, chitosan and etc.) and synthetic ones (poly(lactic acid, PLA), poly(glycolic acid, PLGA) and their copolymer) are preferred [9, 18]. Alginate has been widely used in tissue engineering, growth factor, and cell delivery due to its biocompatible and biodegradable, and was selected as the organic component in this study [26]. Furthermore, 3D printing technique offers a solution of depositing two or three different architectures for biphasic and triphasic scaffolds generally [4, 27–29]. And the scaffold pore structures are prepared through computer-assisted design-computer-aided manufacturing under mild conditions as well [30].

The aim of the present study is to fabricate a triphasic osteochondral scaffold with enhanced interlayer bonding and mechanical properties. Sodium alginate (SA) was used as the main component in all the three layers of scaffolds, which was crosslinked by additional Ca^{2+} after printing to unify separate layers [31, 32]. For the calcified midlayer and subchondral layer, MBG [33, 34] were introduced to form composite with SA and improve the bone-implant integration and strengths of scaffolds.

2 Materials and methods

2.1 Materials

$\text{EO}_{20}\text{PO}_{70}\text{EO}_{20}$ (P123), hydrochloric acid (HCl, 0.5 M), ethyl alcohol ($\text{C}_2\text{H}_5\text{OH}$), tetraethyl orthosilicate (TEOS), triethyl phosphate (TEP), calcium nitrate and ($\text{Ca}(\text{NO}_3)_2 \cdot 4\text{H}_2\text{O}$, 99%) were purchased from Sinopharm Chemical Reagent Co. Ltd. Sodium alginate was purchased from Sigma-Aldrich. All chemicals were used without further purification.

2.2 Synthesis and characterizations of MBG powders

MBG powders were synthesized through an evaporation-induced self-assembly process according to a previous report [35]. After the removal of P123 surfactants, the MBG product was ground and sieved to reduce the particle size to less than $50\ \mu\text{m}$. The mesoporous structure of MBG powder was characterized by transmission electron microscopy (TEM, JEM-2010, 200 kV). N_2 adsorption–desorption isotherms were obtained on a Micromeritics Tristar 3020 at $-196\ ^\circ\text{C}$ under continuous adsorption conditions. Brunauer–Emmett–Tellwe (BET) and Barrett–Joyner–Halenda (BJH) methods were used to determine the surface area, the pore size distribution, and the pore volume.

2.3 Fabrication of triphasic composite scaffolds via 3D printing

Before printing, proper printing pastes including sodium alginate hydrogel and MBG/SA composites were firstly prepared. Typically, SA was completely dissolved in ultrapure water at 95 °C to obtain an 8% (w-v) solution for further use, named as Solution A. Then another 2 g of SA was added into 10 ml of Solution A to increase the viscosity for injection after thoroughly stirring. The other composite paste of MBG and SA was prepared by homogeneously mixing 10 ml Solution A with 1 g of SA powders and 1 g of MBG powders. All raw pastes were sieved again to remove aggregates prior printing.

The pastes were then loaded into polyethylene cartridges (EFD, USA) which were fixed on the 4th generation 3D Bioplotter™ system (EnvisionTEC, Germany). Under the guide of supporting computer workstations, the pastes were extruded at room temperature from the dispensers through the conic plastic nozzles (22G, EFD, USA). A cylinder triphasic scaffold (8 mm of diameter, 5 mm of height) was printed with a strand inter distance of 400 μm by applying compressed nitrogen. Printing gas pressure was controlled in the range of 1.5–3 bar and paste printing speed was in the range of 3–5 mm/s. Specifically, the three parts of triphasic scaffold were designed and printed as follow: according to printing order, the first 8 layers were constructed with SA/MBG paste along interlayer directions of 60° to act as bony phase. The next 2 layers were densely printed with the same SA/MBG pastes to serve as compact separation layers. The top 5 layers of chondral phase in the scaffold were made up of only SA hydrogel paste along interlayer directions of 90°. Finally, the scaffolds were soaked in CaCl₂ solution (50 mg/ml) to cross-link. Samples were kept in fridge for future use.

2.4 Characterizations of scaffolds

Every part of the triphasic scaffolds and the junction areas were observed by scanning electron microscopy (SEM, FEI Quanta 450). The porosities of upper alginate scaffold, lower SA/MBG composite, and the whole triphasic scaffold were measured using Archimedes' principle, and calculated according to the following formulation:

$$P = (W_{sat} - W_{dry}) - (W_{sat} - W_{sus}) \times 100\%$$

where W_{dry} is the dry weight of scaffolds, W_{sus} is the weight of scaffolds suspended in anhydrous ethanol, and W_{sat} is the weight of scaffolds saturated with anhydrous ethanol.

2.5 Mechanical strength properties

The compressive strengths of cylindrical chondral phase scaffolds and bone phase scaffolds ($d = 8$ mm, $h = 5$ mm)

were respectively tested using a Zwick static materials testing machine (2.5 kN) at a crosshead speed of 0.5 mm/min. In addition, SA/MBG scaffolds were dried and then tested as well.

The tensile strength tests of the different scaffold samples (40 × 10 × 1.6 mm), which were directly 3D-printed, were performed using a Zwick static materials testing machine (2.5 kN), moving at a speed of 1 mm/min in the directions parallel to the printed layer. The results were presented as a force-elongation curve and tensile strength was calculated. Same tests were carried out for scaffold samples after they were immersed in SBF or DMEM culture medium for 7 days under 37 °C.

2.6 Interfacial adhesion strengths

Interfacial adhesion strength between the layers of the construct was determined using a single-lap testing. Scaffolds consisting any two phasic parts (SA-SA/MBG scaffold, SA-SA/MBG compact layer, SA/MBG scaffold-SA/MBG compact layer) were printed into a single lapped shape, as Fig. 1 illustrated. The two single-layer ends of sample was fixed to allow secure fixation of scaffold while ensuring correct alignment of the scaffold between the machine's load cell and base plate. Pull force were directly applied to the jig and the forces were recorded till fracture occurred.

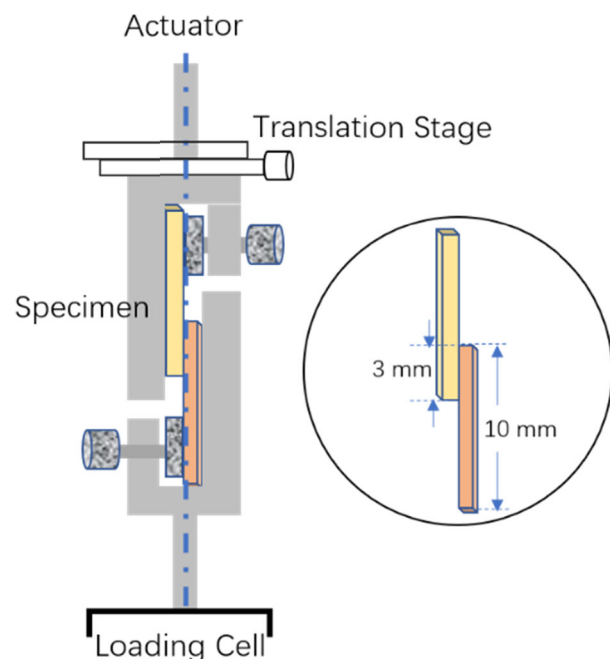


Fig. 1 Configuration of modified single-lap testing. The grips of jig provide lateral support to reduce bond rotation during sample extension

3 Results and discussion

3.1 Characterization of mesoporous bioactive glass

MBG powders synthesized via EISA process showed highly ordered mesoporous channels according to the TEM observation (Fig. 2a), which is coincided to previous result. Figure 2b, c shows N_2 adsorption–desorption isotherms of MBG powders together with the corresponding pore size distributions. The isotherms possessed a typical type IV curve and the type H1 hysteresis loop, indicating the mesoporous structure. The BET surface area was calculated to be about $405 \text{ m}^2/\text{g}$, and the single point adsorption total volume at $P/P_0 = 0.99$ was $0.41 \text{ cm}^3/\text{g}$. The pore size distribution peaked in Fig. 2c at around 3.5 nm which was calculated using the BJH model.

3.2 Characterization of scaffolds

The optical and SEM observations of scaffold layers were displayed in Fig. 3. As it shows, the regular macropores stacking up by printed strands were basically in line with expectations. The upper layers of chondral phase scaffolds possessed interconnected square pore architecture with a

dimension at about $400 \mu\text{m}$, which was consistent with pre-designed parameters. Printed SA filaments showed slight shrinkage due to comparable high viscosity during 3D printing, while the surface of alginate hydrogel was relatively smooth (Fig. 3a). To the contrast, bone phase scaffold exhibited a rough and grainy surface morphology. MBG particles were bound tightly with SA polymers in between. Moreover, on the surface of filaments there were a SA layer wrapping, which was probably attributed to the freeze-drying process. In order to strengthen the scaffold structure, the strands were intersected at 60° in two adjacent layers. Figure 4 shows a cross-section of the developed tri-layered structures. The left dimension in Fig. 4a indicated the cartilage region and the right part corresponded to bone region. These two porous compartments were well separated by a compact layer. In addition, the interface zone was zoomed in as shown in Fig. 4b. It is clearly visible that the three layers were integrated tightly by SA materials. SA macromolecules around the layer interface crosslinked together and provided mechanical interlocking among different regions. The compact middle layer was nonporous as expectation to separate the chondral region and bony region, in that way cartilage and bone regeneration related cells are not allowed to interfere with each other when the scaffolds are put into use [36].

Fig. 2 a TEM image of MBG. b N_2 sorption isotherm and c corresponding pore size distribution of MBG

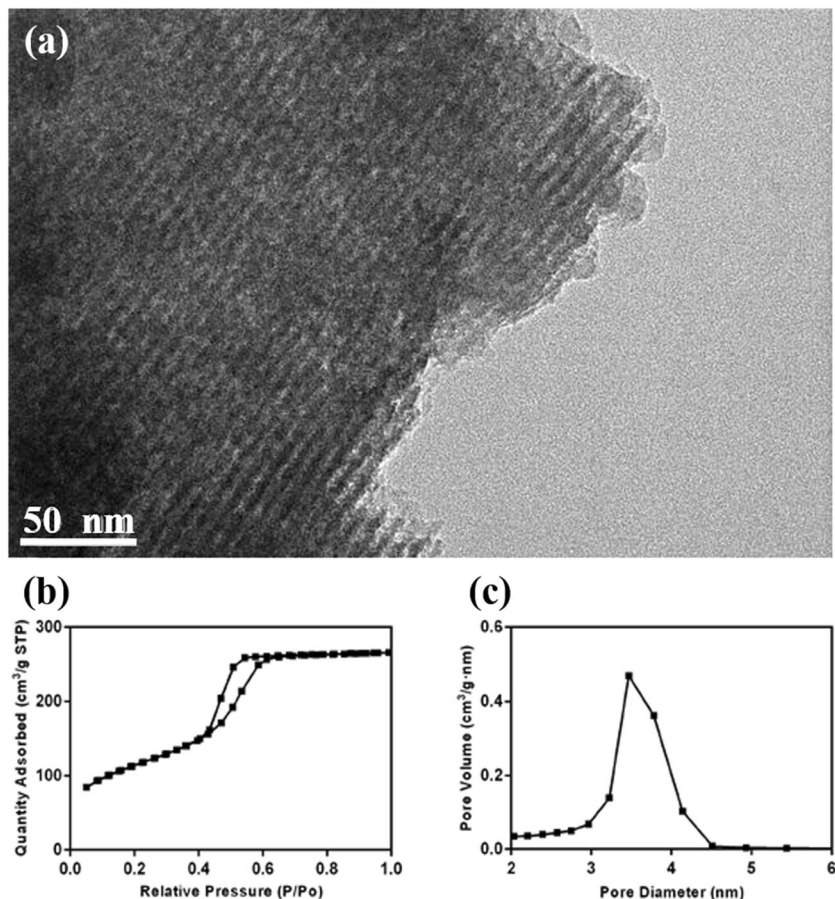


Fig. 3 SEM images of the triphasic composite scaffolds by 3D printing: **a, b** SA, **c, d** SA/MBG

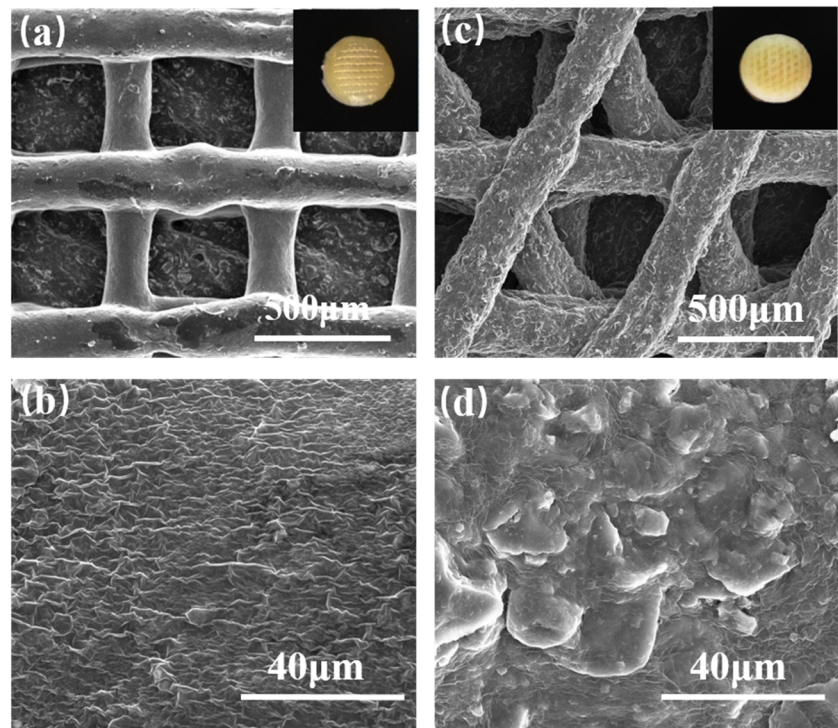


Fig. 4 SEM micrographs showing the longitudinal section of the triphasic scaffold. (an asterisk indicates the chondral phase, symbol “▲” indicates the bony phase and the arrows point to the interface)

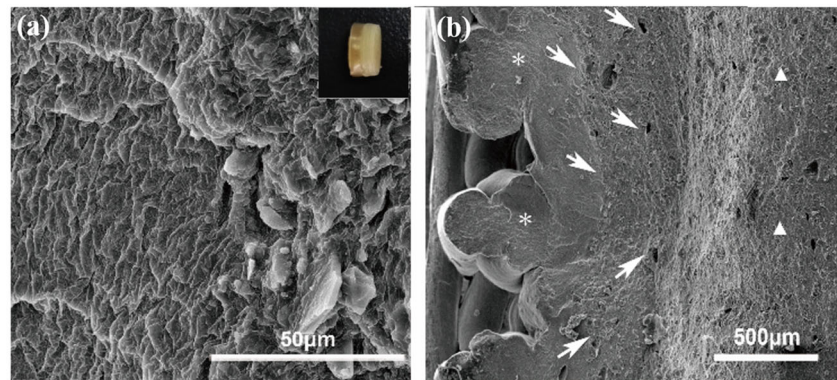


Table 1 Porosity of individual SA scaffold, SA/MBG scaffold, and the triphasic scaffold

Sample	SA	SA/MBG	Triphasic
Porosity (%)	70.29 ± 1.09	74.35 ± 0.54	73.89 ± 0.38

Table 1 shows porosities of solely SA scaffold part, SA/MBG composite scaffold part, and the whole triphasic scaffold. The porosities were estimated at $70.29 \pm 1.09\%$, $74.35 \pm 0.54\%$, and $73.89 \pm 0.38\%$, respectively, which were coincided with 76.25% theory porosity calculated from strand diameters and strand gaps of the two structured scaffold regions. Therefore, 3D printing can generate more complex pore architectures of scaffolds by changing the deposition angles without a significant variety of porosities.

3.3 Mechanical properties of scaffolds

The compressive capacity of SA/MBG bony region in the triphasic scaffolds before and after drying was investigated respectively by compression testing. As shown in Fig. 5a, pictures of scaffolds after compression displayed two entirely different states. Cylindrical wet SA/MBG sample was gradually pressed down to a compacted scaffold with a lower porosity. There was no scaffold rupture and thus the compressive stress value at the end of linear stress-strain relationship curves was recorded as its strength (1.22 ± 0.14 MPa). However, the dried SA/MBG scaffolds broke down under the peak load as failure strength. And the compressive strength was recorded at about 23.47 ± 0.55 MPa. As for the pure SA scaffold, the compression strength was even lower since the water-rich hydrogel

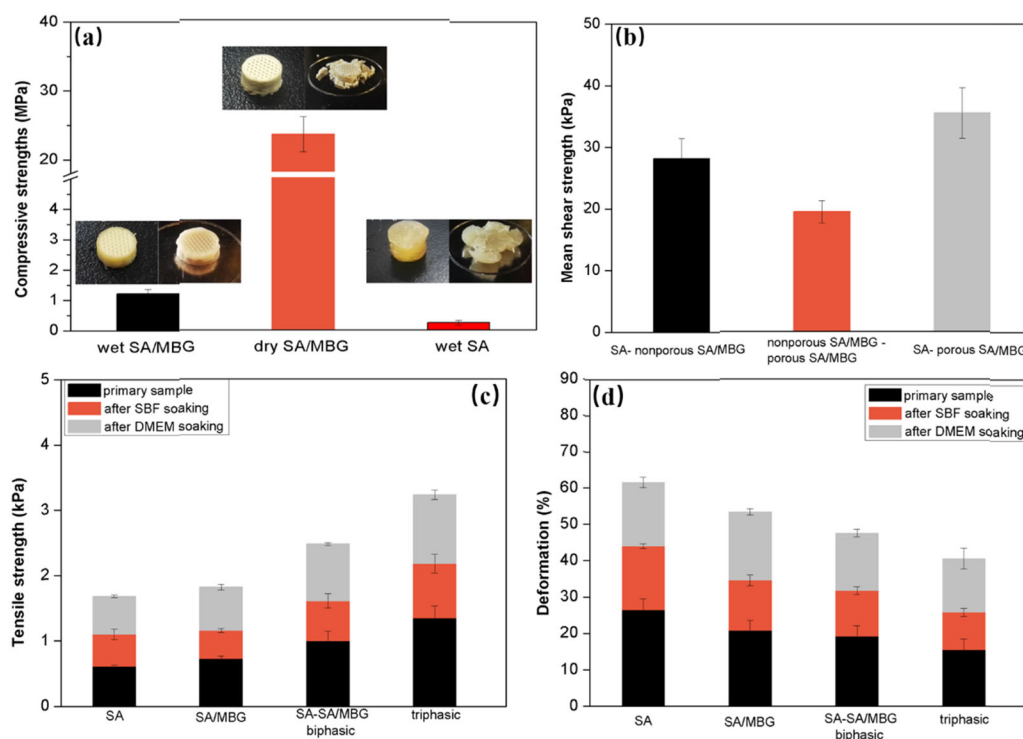


Fig. 5 **a** Compressive strength of wet SA/MBG scaffold, dry SA/MBG scaffold, and wet SA scaffold. The inset photos show appearances before (left) and after (right) the compressive tests. **b** The interfacial strengths between any two scaffold phases including SA-nonporous SA/MBG, nonporous SA/MBG-porous SA/MBG, and SA-porous SA/

MBG. **c** Tensile strengths of the SA, SA/MBG, SA-SA/MBG, and triphasic scaffolds before and after soaking in DMEM or SBF for 7 days. **d** corresponding deformations of the scaffolds when fracture occurred

scaffold collapsed once the loading force arriving at about 0.23 ± 0.08 MPa, although it already reached the minimum 150 kPa of strength as required for cartilage regeneration.

The integration strengths between any two layers (bone, intermediate, and cartilage layers) were tested via shear testing. The maximal fracture strength was recorded as the interface strength. From the results shown in Fig. 5b, any one of the interlayer adhesions were much higher than that of individual layers, that is, the fracture did not happen at the single-layer regions before peeling off. The interface strength between SA scaffold and porous SA/MBG scaffold was larger compared to the other two groups. And to the opposite the interface strength between the dense midlayer and porous SA/MBG scaffolds was the lowest one. Therefore, it can be concluded that higher SA content at the interface caused stronger interface bonding, which implied that SA/MBG multilayer scaffolds here enhanced the interlayer adhesion strengths mainly by SA integration in every scaffold phase. In previous studies, completely different materials in different layers led to insufficient interface strength and bonding, and here the study offered a graded scaffolds of suitable material functions in each scaffold phase with better interface strengths.

Tensile strengths of scaffolds before and after soaking in SBF or DMEM culturing media were investigated

respectively. As listed in Fig. 5c, composite scaffolds compared to SA alone showed increased tensile strengths, and among them the triphasic scaffold possessed the highest value which is almost as twice as SA scaffold. Correspondingly, the elongation length at break decreased with increasing strength (Fig. 5d). That is to say, the triphasic scaffold exhibited the lowest elongation when bearing the same stretch force. Notably, the hydrated condition after soaking either in SBF or DMEM most closely represents the end-use state in clinic. The tensile strengths of all scaffolds after soaking showed substantial decrease due to degradation or swelling. Crosslinked SA absorbed more water and dilated afterwards so that SA network was loosened. Therefore, MBG-containing scaffolds, either SA/MBG or the triphasic integrated scaffolds, displayed higher tensile strengths. On the other hand, in SBF the ionic environment induced both ion dissolutions from MBG component and ion exchanges as well. Ca^{2+} ions dissolved rapidly into the soaking media due to their weak associations with silica network, and then nucleation sites of bone-like apatite were produced [37]. However, SA molecules after crosslinking are naturally capable of providing nucleation sites of Ca^{2+} . Therefore, both of sole SA scaffolds and SA/MBG scaffolds could induce apatite deposition when immersing in the SBF. The surface observation images were shown in Fig. 6.

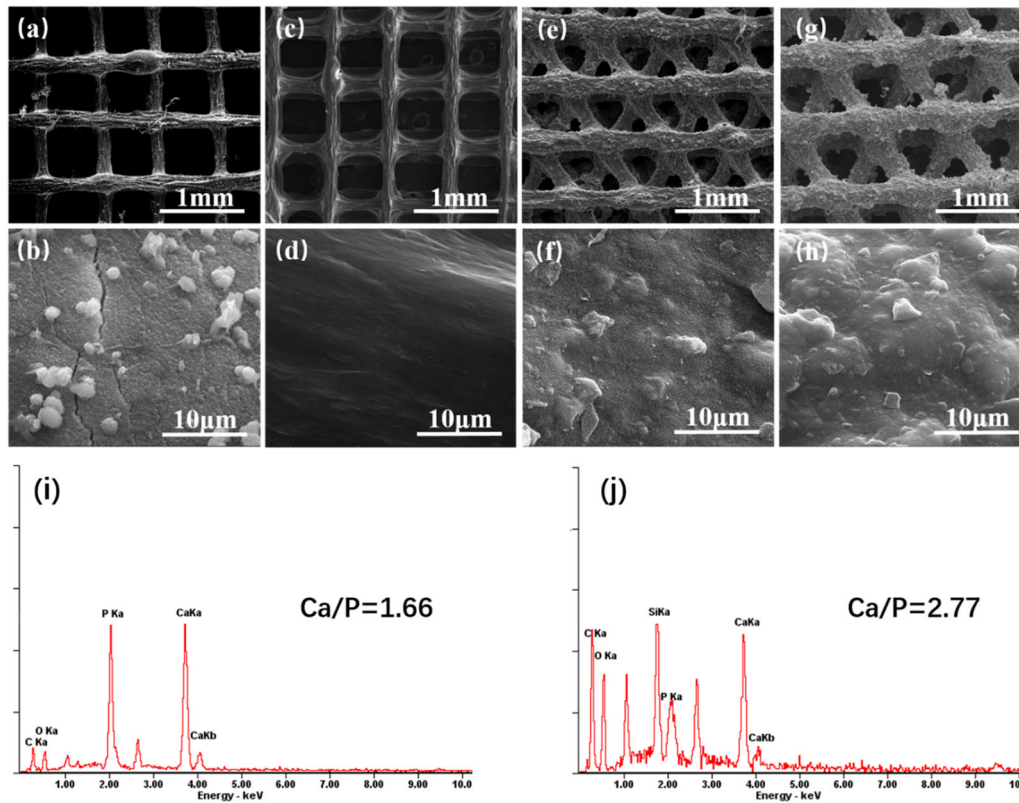


Fig. 6 SEM images of **a, b** SA scaffolds and **e, f** SA/MBG scaffolds after soaking in SBF for 7 days. SEM images of **c, d** SA scaffolds and **g, h** SA/MBG scaffolds after soaking in DMEM for 7 days. EDS spectrum of **i** SA scaffolds and **j** SA/MBG scaffolds after soaking in SBF for 7 days

Additional EDS analysis in Fig. 6i, j showed the surface compositions of SA scaffolds and SA/MBG scaffolds after soaking in SBF for 7 days. Characteristic peaks of Ca and P elements were observed for surface examination of SA scaffolds. The Ca/P molar ratio is determined to be 1.66, that is almost the same with stoichiometric Ca/P (1.67) of hydroxyapatite. However, the Ca/P ratio obtained from the EDS spectrum of SA/MBG scaffolds was 2.77. It was much higher due to the large content of calcium in MBG itself. Therefore we can conclude that apatite mineralization on the surfaces of these scaffolds. Moreover, Fig. 6c, d, g, h also gave solid evidences that DMEM soaking did not cause scaffold disintegration even as long as 7 days, although a slight swelling was not avoided.

4 Conclusions

In this study, we have designed and constructed a tri-layered graded SA/MBG scaffold for osteoarticular regeneration using a multi-nozzle 3D printing technique. By taking the advantages of 3D printing, different combinations of SA macromolecules and MBG bio-inorganics and scaffold architectures were appropriately arranged in different layers. The same SA composition in all layers anchored MBG together and

integrated the whole multilayered scaffolds. Finally, improved mechanical interface bonding strengths were achieved and that suggests promising applications for osteoarticular tissue engineering with further biological studies.

Acknowledgements The authors gratefully acknowledge support a grant from the Shanghai Natural Science Foundation (No.19ZR1435100) and National Natural Science Foundation of China (No.51673212).

Compliance with ethical standards

Conflict of interest The authors declare that they have no conflict of interest.

Publisher's note Springer Nature remains neutral with regard to jurisdictional claims in published maps and institutional affiliations.

References

- Hunziker EB. Articular cartilage repair: basic science and clinical progress, a review of the current status and prospects. *Osteoarthr Cartil.* 2002;10:432–63.
- Pan J, Zhou X, Li W, Novotny JE, Doty SB, Wang L. In situ measurement of transport between subchondral bone and articular cartilage. *J Orthop Res.* 2010;27:1347–52.
- Cole BJ, Busam M. Surgical management of articular cartilage defects in the knee. *J Bone Jt Surg Am.* 2009;91:1778–90.

4. Levingstone TJ, Matsiko A, Dickson GR, O'Brien FJ, Gleeson JP. A biomimetic multi-layered collagen-based scaffold for osteochondral repair. *Acta Biomater*. 2014;10:1996–2004.
5. Zhang L, Hu J, Athanasiou KA. The role of tissue engineering in articular cartilage repair and regeneration. *Crit Rev Biomed Eng*. 2009;37:1–57.
6. Tamaddon M, Wang L, Liu Z, Liu C. Osteochondral tissue repair in osteoarthritic joints: clinical challenges and opportunities in tissue engineering. *Bio-Des Manuf*. 2018;1:101–14.
7. Jia S, Wang J, Zhang T, Pan W, Li Z, He X. Multilayered scaffold with a compact interfacial layer enhances osteochondral defect repair. *ACS Appl Mater Inter*. 2018;10:20296–305.
8. Longley R, Ferreira AM, Gentile P. Recent approaches to the manufacturing of biomimetic multi-phasic scaffolds for osteochondral regeneration. *Int J Mol Sci*. 2018;19:1755.
9. Holmes B, Zhu W, Li J, Lee JD, Zhang LG. Development of novel three-dimensional printed scaffolds for osteochondral regeneration. *Tissue Eng Part A*. 2015;21:403–15.
10. Kang H, Zeng YZ, Varghese S. Functionally graded multilayer scaffolds for in vivo osteochondral tissue engineering. *Acta Biomater*. 2018;78:365–77.
11. Engler AJ, Sen S, Sweeney HL, Discher DE. Matrix elasticity directs stem cell lineage specification. *Cell*. 2006;126:677–89.
12. Nukavarapu SP, Dorcenus DL. Osteochondral tissue engineering: current strategies and challenges. *Biotechnol Adv*. 2013;31:706–21.
13. Levingstone TJ, Ramesh A, Brady RT, Brama PAJ, Kearney C, Gleeson JP. Cell-free multi-layered collagen-based scaffolds demonstrate layer specific regeneration of functional osteochondral tissue in caprine joints. *Biomaterials*. 2016;87:69–81.
14. H Da, S Jia, G Meng, J Cheng, W Zhou, Z Xiong. The impact of compact layer in biphasic scaffold on osteochondral tissue engineering. *Plos One*. 2013;8. <https://doi.org/10.1371/journal.pone.0054838>.
15. Sachlos E, Czernuszka JT. Making tissue engineering scaffolds work. Review: the application of solid freeform fabrication technology to the production of tissue engineering scaffolds. *Eur Cells Mater*. 2003;5:29–39.
16. Klein TJ, Malda J, Sah RL, Huttmacher DW. Tissue engineering of articular cartilage with biomimetic zones. *Tissue Eng Part B*. 2009;15:143–57.
17. Harley BA, Lynn AK, Wissner-Gross Z, Bonfield W, Yannas IV, Gibson LJ. Design of a multiphase osteochondral scaffold III: fabrication of layered scaffolds with continuous interfaces. *J Biomed Mater Res A*. 2010;92:1078–93.
18. Chen GP, Tanaka J, Tateishi T. Osteochondral tissue engineering using a PLGA-collagen hybrid mesh. *Mat Sci Eng C-Bio S*. 2006;26:124–9.
19. Huang T, Fan C, Zhu M, Zhu Y, Zhang W, Li L. 3D-printed scaffolds of biomaterialized hydroxyapatite nanocomposite on silk fibroin for improving bone regeneration. *Appl Surf Sci*. 2019;467:345–53.
20. Li L, Hu H, Zhu Y, Zhu M, Liu Z. 3D-printed ternary SiO₂-CaO-P₂O₅ bioglass-ceramic scaffolds with tunable compositions and properties for bone regeneration. *Ceram Int*. 2019;45:10997–1005.
21. Du X, Fu S, Zhu Y. 3D printing of ceramic-based scaffolds for bone tissue engineering: an overview. *J Mater Chem B*. 2018;6:4397–412.
22. Moxon SR, Cooke ME, Cox SC, Snow M, Jeys L, Jones SW, Smith AM, Grover LM. Suspended manufacture of biological structures. *Adv Mater*. 2017;29:1605594.
23. Rotbaum Y, Puiu C, Rittel MD. Quasi-static and dynamic in vitro mechanical response of 3D printed scaffolds with tailored pore size and architectures. *Mater Sci Eng*. 2019;96:176–82.
24. Roseti L, Parisi V, Petretta M, Cavallo C, Desando G, Bartolotti L, Grigolo B. Scaffolds for bone tissue engineering: state of the art and new perspectives. *Mater Sci Eng C*. 2017;78:1246–62.
25. Zhao S, Zhang J, Zhu M, et al. Effects of functional groups on the structure, physicochemical and biological properties of mesoporous bioactive glass scaffolds. *J Mater Chem B*. 2014;3:1612–23.
26. Zhao F, Zhang W, Fu X, Xie W, Chen X. Fabrication and characterization of bioactive glass/alginate composite scaffolds by a self-crosslinking processing for bone regeneration. *RSC Adv*. 2016;6:91201–8.
27. Castro NJ, O'Brien J, Zhang L. Integrating biologically inspired nanomaterials and table-top stereolithography for 3D printed biomimetic osteochondral scaffolds. *Nanoscale*. 2015;7:14010–22.
28. Shim JH, Jang KM, Hahn SK, Park JY, Jung H, Oh K. Three-dimensional bioprinting of multilayered constructs containing human mesenchymal stromal cells for osteochondral tissue regeneration in the rabbit knee joint. *Biofabrication*. 2016;8:014102.
29. Gao F, Xu Z, Liang Q, Liu B, Li H, Wu Y. Direct 3D printing of high strength biohybrid gradient hydrogel scaffolds for efficient repair of osteochondral defect. *Adv Funct Mater*. 2018;28:1706644.
30. Domingos M, Chiellini F, Gloria A, Ambrosio L, Bartolo PJ, Chiellini E. BioExtruder: study of the influence of process parameters on PCL scaffolds properties. In: Bartolo PJ, (ed.). *Innovative developments in design and manufacturing—advanced research in virtual and rapid prototyping*. Oxford: Taylor & Francis; 2009. p. 67–73.
31. Augst AD, Kong HJ, Mooney DJ. Alginate hydrogels as biomaterials. *Macromol Biosci*. 2006;6:623–33.
32. Stagnaro P, Schizzi I, Utzeri R, Marsano E, Castellano M. Alginate-polymethacrylate hybrid hydrogels for potential osteochondral tissue regeneration. *Carbohydr Polym*. 2018;185:56–62.
33. Zhu M, Zhang J, Zhao S, Zhu Y. Three-dimensional printing of cerium-incorporated mesoporous calcium-silicate scaffolds for bone repair. *J Mater Sci*. 2016;51:836–44.
34. Cai L, Lin D, Chai Y, Yuan Y, Liu C. MBG scaffolds containing chitosan microspheres for binary delivery of IL-8 and BMP-2 for bone regeneration. *J Mater Chem B*. 2018;6:4453–65.
35. Yan X, Yu C, Zhou X, Tang J, Zhao D. Highly ordered mesoporous bioactive glasses with superior in vitro bone-forming bioactivities. *Angew Chem Int Ed*. 2004;43:5980–4.
36. Martin I, Miot S, Barbero A, Jakob M, Wendt D. Osteochondral tissue engineering. *J Biomech*. 2007;40:750–65.
37. Ramaswamy Y, Wu C, Zhou H, Zreiqat H. Biological response of human bone cells to zinc-modified Ca-Si-based ceramics. *Acta Biomater*. 2008;4:1487–97.